

RSC Advances



This is an *Accepted Manuscript*, which has been through the Royal Society of Chemistry peer review process and has been accepted for publication.

Accepted Manuscripts are published online shortly after acceptance, before technical editing, formatting and proof reading. Using this free service, authors can make their results available to the community, in citable form, before we publish the edited article. This *Accepted Manuscript* will be replaced by the edited, formatted and paginated article as soon as this is available.

You can find more information about *Accepted Manuscripts* in the [Information for Authors](#).

Please note that technical editing may introduce minor changes to the text and/or graphics, which may alter content. The journal's standard [Terms & Conditions](#) and the [Ethical guidelines](#) still apply. In no event shall the Royal Society of Chemistry be held responsible for any errors or omissions in this *Accepted Manuscript* or any consequences arising from the use of any information it contains.

**Structure and Hydrothermal Stability of Highly Oriented
Polyamide 6 Produced by Solid Hot Stretching**

Kaihua Shi, Lin Ye*, Guangxian Li

Corresponding author: Lin Ye

Address: State Key Laboratory of Polymer Materials Engineering

Polymer Research Institute of Sichuan University, Chengdu 610065, China

E-mail: yelinwh@126.com

Tel: 86-28-85408802

Fax: 86-28-85402465

Structure and Hydrothermal Stability of Highly Oriented Polyamide 6 Produced by Solid Hot Stretching

Kaihua Shi, Lin Ye*, Guangxian Li

State Key Laboratory of Polymer Materials Engineering
Polymer Research Institute of Sichuan University, Chengdu, 610065, China

Abstract: Highly oriented polyamide 6 (PA6) was successfully fabricated through solid hot stretching technology. The effect of orientation on the structure and hydrothermal stability of PA6 was investigated. It was found that molecular orientation reduced the hydrophilicity of PA6 and restricted the water uptake, and therefore hindered molecular hydrolytic degradation. The α crystalline form mainly formed for the oriented PA6. With the increase of draw ratio, the crystallinity and orientation factor of PA6 increased, the fractional free volume (f_v) decreased, and a dense crystalline structure was formed. During aging, the crystalline form of PA6 changed from γ to α , and thus compared with the isotropic sample, the oriented sample can keep relatively stable dense crystalline structure, which was favorable for the inhibition of water diffusion into PA6, and slowing down the hydrolytic degradation. This investigation clearly showed that molecular orientation can be an efficient way to enhance the hydrothermal stability of PA6.

Keywords: Polyamide 6 (PA6); Molecular orientation; Hydrothermal stability; Microstructure

1. Introduction

Polyamide 6 (PA6), as one of the most common engineering plastics, has a wide range of applications in industry due to its excellent mechanical properties, oil resistance, and abrasive resistance [1, 2]. However, amide groups in the backbone of

PA6 are sensitive to moisture environment, and undergo a reversible hydrolysis reaction, resulting in obvious deterioration of chemical structures and physical performances, and consequently limiting the use of polyamide materials [3-5]. The degradation of polyamides when exposed to water has been examined by some scholars [5-7]. A common aspect of these researches focused on degradation-dependent changes in mechanical properties, sample weight and water diffusion. N.S. Murthy et al. [6] found that water molecules diffused almost exclusively into the amorphous regions of PA6. Diffusion of water into the interlamellar regions swelled this amorphous matrix, increased the lamellar repeat, decreased the unit cell volume in preexisting lamellae, and at elevated temperatures hydrolyzed the tie molecules. D.P.N. Vlasveld [7] et al. studied the moisture absorption in PA6 silicate nanocomposites and its influence on the mechanical properties. They found that the nanocomposites absorbed water at a slower rate than the unfilled PA6 samples, and the modulus would eventually drop after enough moisture was absorbed. In a more recent study, Shu et al. [5] studied the aging behavior of PA6 under acid rain in terms of water absorption behavior, mechanical property, chemical structure, and appearance properties. The stabilization of PA6 mostly focused on the thermal-oxidative and ultraviolet-oxidative stabilization [8-11], while few literatures on hydrothermal stabilization can be available for PA6.

Polymer secondary structure such as chain crystalline and orientation has significant effect on its stability and aging behavior [12-14]. Eldsater C et al. [12] found that selective degradation induced by extra cellular enzymes occurred in the amorphous part of oriented poly (ϵ -caprolactone) (PCL) films prior to the crystalline structure. Do Kwang Cho et al. [13] studied the effect of molecular orientation on biodegradability of poly(glycolide-co- ϵ -caprolactone) (PGCL), and found that the

degradation decreased with increasing draw ratio. Zhou Y et al. [14] investigated the effect of crystallization on hydrolytic stability of polycarbonate (PC) and confirmed that solvent-induced crystallization on surface can be an efficient way to enhance the hydrolytic stability of PC.

In this work, highly oriented PA6 was successfully fabricated through solid hot stretching technology. The effect of orientation on the structure and hydrothermal stability of PA6 was investigated for the first time, and the enhancing mechanism of hydrothermal stability of PA6 was also explored.

2. Experimental

2.1 Materials

PA6 used in this work is a commercial grade granular product (YH800) without any additives and supplied by Yueyang Petrochemical Co. (Hunan, China), with relative viscosity of 2.85 ± 0.03 . All the other solvents and reagents were used as-received.

2.2 Preparation of the oriented PA6

Sample Preparation: PA6 particles were dried at 90 °C for 12 h in a vacuum oven before processing, and then pressed into 2.0 mm thick films under 10 MPa pressure at 250 °C, followed by cooling process at room temperature. Finally the films were cut into standard dumb-bell splines for drawing.

Drawing: The dumb-bell splines of PA6 were drawn on the self-made hot stretching apparatus at 170 °C and the stretching rate was fixed at 25 mm/min. The draw ratio (DR) of the sample was determined with the following equation:

$$DR = 100 \times \frac{L - L_0}{L_0} \quad (1)$$

where L_0 is the sample length prior to drawing and L is the final length after drawing. After the desired DR was obtained, the sample was cooled down to room temperature, and then the load was released.

2.3 Hydrothermal aging

Pre-weighed samples of PA6 (W_0) were immersed in separate beakers containing 500 mL deionized water at a constant temperature of 85 °C. At predetermined periods, the PA6 samples were picked out and wiped with filter paper to remove surface water. The wet weight (W_w) was measured immediately, and these specimens were then dried to a constant weight at 40 °C to weigh again (W_d).

The water absorption and the weight gain of PA6 samples were obtained with the following equations.

$$\text{Water absorption(\%)} = 100 \times \frac{W_w - W_d}{W_d} \quad (2)$$

$$\text{Weight change(\%)} = 100 \times \frac{W_0 - W_d}{W_0} \quad (3)$$

2.4 Characterization

Static water contact angle measurements of the PA6 samples were conducted with DSA30 Krüss contact angle goniometer (KRÜSS GmbH, Germany) at 25 °C and 50% RH. Average values of contact angles were deduced from a total of at least ten measurements on different areas of each specimen.

The intrinsic viscosities $[\eta]$ of the PA6 samples were measured with an Ubbelohde viscometer at 25 °C in formic acid at approximately 0.5% polymer concentration through a single point method according to the following equation:

$$[\eta] = \frac{\sqrt{2(\eta_{sp} - \ln \eta_r)}}{c} \quad (4)$$

where η_r is relative viscosity, $\eta_{sp}=\eta_r - 1$ is specific viscosity and c is polymer solution concentration [15]. Intrinsic viscosity can be related to viscosity-average molecular weight (\overline{M}_η) through the Mark–Houwink equation:

$$[\eta]=K(\overline{M}_\eta)^\alpha \quad (5)$$

where the values of K and α are, respectively, 7.2×10^{-2} and 0.70 for PA6.

The mechanical properties of PA6 samples were measured by Instron 5567 material testing machine (Instron Co., USA) according to ISO 527-1:2012(E). The test speed was 20 mm/min, and the sample length between benchmarks was 20 mm.

Dynamic mechanical analysis (DMA) of PA6 samples was performed by using a TA Instrument Q800 DMA (TA Instruments, USA). Samples were analyzed over the temperature range of -100 °C to 150 °C at a heating rate of 3 °C/min and a frequency of 1 Hz in a strain mode. The sample size was 14 mm in length.

Microstructures of the PA6 samples were recorded with JSM-5900LV scanning electron microscope (SEM) (JEOL Ltd., Japan) with an acceleration voltage of 20 kV. Before SEM observation, the samples were sputter-coated with gold for 2–3 min.

The thermal properties of PA6 samples were performed with a Netzsch 204 differential scanning calorimetry (DSC) (Phoenix Co, Germany). The temperature scale of DSC was calibrated with indium. Granulated samples of about 10 mg were heated from ambient temperature to 250 °C at a constant rate of 10 K/min under nitrogen atmosphere. The crystallinity (X_c) can be calculated with the following equation:

$$X_c=(\Delta H_m/\Delta H_0) \times 100\% \quad (6)$$

where ΔH_m is the melting enthalpy and ΔH_0 is the melting enthalpy of 100% crystalline PA6, which is 190 J/g [16].

Two-dimensional wide-angle X-ray diffraction (2D-WAXD) analysis was conducted at ambient temperature using a D8 Discover two-dimensional wide angle X-ray diffractometer (Bruker AXS Co, Germany). The sampling time of 2D -WAXD measurements was 180 s using an Eulerian 1/4 cradle HI-STAR (2D-Detector) detector, with a wavelength of 0.154 nm monochromated X-ray obtained from Cu (K_{α}) radiation.

The positron annihilation lifetime spectroscopy (PALS) of PA6 samples were measured by a conventional fast-fast coincidence spectrometer at room temperature. A 30 μ Ci 22 Na positron source sealed between two sheets of nickel foil (1 mg/cm²) was sandwiched between two pieces of the samples. About 10⁶ data points were collected per spectrum. The third component ($\tau_3 \approx 1-3$ ns) originated from orthopositronium interacts with the surrounding electron densities and showed systematic variation with free volume. The lifetime and intensity of τ_3 can be used to illustrate the size and concentration of free volume holes.

3. Results and discussion

3.1 Hydrothermal aging behavior of the oriented PA6

3.1.1 Water absorption behavior and weight gain during hydrothermal aging

The water absorption is somewhat related to the hydrolytic degradation when specimens are in contact with an aqueous medium. Fig. 1 shows the evolution of water absorption of PA6 as a function of hydrothermal aging time at immersion temperature of 85 °C. There were two distinct chronological regimes. At the initial stage, the water diffused quickly into the PA6 matrix, following the Fick's second law, and the diffusion rate decreased with the draw ratio. Each sample reached their water saturation at the second regime and the equilibrium water absorption ratio decreased with the increase of draw ratio. The water absorption increase for the isotropic sample

and the oriented sample (DR-200%) of PA6 after 30 days may be due to the polymer hydrolysis, producing more hydrophilic carboxyl groups and amine groups [17].

Fig. 1

Theoretically, for the boundary condition, when the concentration of the solution on the surface of sample is constant and no chemical reaction occurs during the process of immersion, water absorption should be a Fick's process, which can be characterized by a constant coefficient of diffusion (D) and an equilibrium saturation water absorption (M_∞), and obeying the following relationship [18]:

$$\frac{M_t}{M_\infty} = 1 - \frac{8}{\pi^2} \sum_{n=0}^{\infty} \frac{1}{(2n+1)^2} \exp\left[-\frac{(2n+1)^2 \pi^2 D}{L^2} t\right] \quad (7)$$

In the initial process of immersion, the curve should have a good linear relationship as per the following formula:

$$\frac{M_t}{M_\infty} = \frac{4}{\sqrt{\pi}} \sqrt{\frac{Dt}{L^2}} \quad (8)$$

Then, water absorption (M_t) of PA6 was further plotted vs $t^{1/2}/L$ (L being the sample thickness), as shown in Fig. 2. Equation (8) was fitted to the experimental data using a linear regression analysis at a level of confidence of 95%. According to the slope of line, D could be calculated when M_∞ was determined and summarized in Tab. 1. The value of D for the isotropic sample was much higher than that of the oriented sample and decreased with the draw ratio. The orientation of PA6 reduced the mobility of polymer chains, and restricted the water uptake and swelling at the early stage of the aging process. Thus the hydrolytic degradation maybe inhibited to a certain degree [19].

Fig. 2

Tab. 1

Figure 3 shows the weight gain (%) as a function of hydrothermal aging time for all PA6 samples. At first, the weight of the samples increased as a result of the hydrolysis of the amide groups of PA6. The incorporation of 1 mol H₂O to the polymer, i.e. 18g, per hydrolysis event was expected. The isotropic sample showed the most rapid increase in weight, and reached maximum in about 3 hours. Afterwards, the weight of the isotropic sample and the sample with 200% draw ratio began to drop sharply, indicating that lots of low molecular weight compounds were extracted from the matrix and dissolved in water. However, the weight dropped very slowly for the samples with higher draw ratio, indicating that orientation can inhibit the hydrolytic degradation of PA6.

Fig. 3

3.1.2 Intrinsic viscosity during hydrothermal aging

It is well known that the intrinsic viscosity characterizes the viscosity average molecular weight of polymers. The variation of the intrinsic viscosity of the samples of PA6 with aging time is shown in Fig. 4. The intrinsic viscosity was found to decrease monotonously with time for all PA6 samples. Compared with the isotropic sample, a much slow drop of the intrinsic viscosity was observed for the oriented samples.

Fig. 4

A model accounting for autocatalysis by the generated carboxylic acid end groups is described with the following rate equation [20]:

$$\overline{M}_{nt} = \overline{M}_{n0} e^{-kt} \quad (9)$$

where k is catalyzed hydrothermal degradation rate constant.

Based on the Mark–Houwink equation (Eq. (5)), $[\eta]$ is related to the viscosity average molecular weight, \overline{M}_η , which is proportional to \overline{M}_n [21]. Therefore, Eq. (9) can be converted into an equation incorporating $[\eta]$,

$$\ln\left(\frac{[\eta]}{[\eta]_0}\right) = -k_1 t \quad (10)$$

where k_1 is the $[\eta]$ catalyzed hydrothermal degradation rate constant, which can be determined by linear regression from plots of $\ln([\eta]/[\eta]_0)$ vs. aging time at 85 °C (Fig. 5). The degradation rate constant (k_1) and the corresponding correlation coefficients (R^2) for PA6 samples are shown in Tab. 2. The high correlation coefficients support the validity of the autocatalytic degradation mechanism. It can be seen that the degradation rate constant decreased with the increase of draw ratio, indicating that molecular orientation of PA6 contributed to slowing down the hydrolysis-induced backbone cleavage.

Fig. 5

Tab. 2

3.1.3 Mechanical properties during hydrothermal aging

The variation of mechanical properties of PA6 with aging time is shown in Fig. 6. In the initial stage of aging, lots of water diffused into the PA6 matrix, functioning as plasticizers and resulting in a decrease of the tensile strength and an increase of the elongation at break of PA6. However, with the continuing of aging, the molecular weight of the sample decreased gradually, which finally resulted in the decline of mechanical properties of the isotropic sample of PA6, which tensile strength and elongation at break dropped to below 50% after 30 days' hydrothermal aging. However, the oriented samples of PA6 kept much more stable and higher mechanical properties during hydrothermal aging.

Fig. 6**3.1.4 Surface morphology during hydrothermal aging**

As shown in Fig. 7. With the increase of aging time, the samples gradually turned yellow, indicating that chromophore structure was generated. With increase of draw ratio, the time of yellowing was postponed, indicating that the formation of chromophore structure was inhibited. The discoloration of PA6 resulted from the formation of chromophore-ketoamide groups through oxidation of the methylene group adjacent to the carbonyl of the amide [22].

Fig. 7

The surface morphology of PA6 during the hydrothermal aging with varying draw ratio was shown in Fig. 8. It can be seen that the non-hydrolyzed undrawn PA6 samples showed a relatively smooth surface. As the draw ratio increased, the initial structure became more elongated along the principal tensile strain axis, and the micro-fibers structure was formed. Compared with the oriented samples, much more and wider cracks were observed for the isotropic sample during aging, while no obvious surface destruction occurred for the sample with DR-600%. Moreover, it's worth noting that more micro-fibers structure formed after hydrothermal aging for the oriented samples, suggesting that the erosion by hydrolysis occurred preferentially in the less ordered amorphous region between the oriented fibrils formed along the drawing direction.

In this work, the cracks arranged parallel to the fiber texture at first and then perpendicular to the fiber texture. The amorphous region between lamellae became considerably weak and easily cracked along the lamellar direction by the selective degradation through the penetrating force of water into interlamellar region. The start

of crystallization region degradation after complete hydrolysis of the amorphous regions perhaps led the cracks to arrange perpendicular to the fiber texture.

Fig. 8

3.2 Hydrothermal stabilizing mechanism of the oriented PA6

3.2.1 Surface property

Figure 9 showed the water contact angles of PA6 as a function of draw ratio. It can be seen that the water contact angles increased with increasing draw ratio, indicating that orientation could enhance the hydrophobicity of PA6 obviously. The variations in the hydrophobicity could be ascribed to the increase of surface roughness and enhancement of intermolecular interaction [23-25].

Fig. 9

3.2.2 Orientation and crystallization properties

To observe the crystal structure of PA6 after drawing, the samples of PA6 was etched in hot water for a certain period of time and observed by SEM. As shown in Fig. 10, the spherulitic structure present in the initial isotropic sample was completely absent in the drawn PA6 sample, and the mat texture crystals were observed. Through drawing, the lamellar structure that formed the original spherulitic morphology was broken up, and the folded-chain crystalline blocks were torn from the lamellar. The crystalline blocks were connected by taut tie molecules, which originated from partial unfolding of chains, and formed long microfibrils aligned in the draw direction [26].

Fig. 10

The DSC thermograms of isotropic and drawn samples of PA6 were shown in Fig. 11, from which the melting temperature (T_m), the heat of melting (ΔH_m) and the crystallinity (X_c) can be obtained, as listed in Tab. 3.

The melting endotherm of an isotropic PA6 sample exhibited a peak around 222 °C and an additional small shoulder peak at the lower temperature side of the melting peak was observed, and the cold crystalline was very obvious, indicating the imperfect crystallization of the sample. However, for the oriented sample, the shoulder peak and cold crystalline disappeared, and the melting temperature (T_m) decreased with the draw ratio, indicating the perfect crystallization of the sample, and the transformation of crystalline form γ to α because the crystalline form α with a more stable crystalline structure than crystalline form γ has a relatively low melting temperature [27]. In addition, with the increase of draw ratio, the melting enthalpy and crystallinity of PA6 increased, as shown in Tab. 3, indicating of the stress-induced crystallization of PA6 during drawing.

Fig. 11

Tab. 3

The 2D-XRD patterns of the PA6 during the hydrothermal aging with varying draw ratio were shown in Fig. 12. The isotropic sample before drawing presented a series of uniform Debye-Scherrer diffraction rings due to the random arrangement of grains. While for the samples oriented, the (200) and (002)/(202) reflection appeared as two strong circular spots on the equator. With increasing draw ratio, these arcs became narrower in spread and more prominent, suggesting that the crystal axis was preferentially oriented perpendicular to the draw direction. With increase of aging time, the (200) and (002)/(202) reflection of PA6 became more prominent, suggesting that during aging the degree of the order of PA6 increased.

Fig. 12

One-dimensional X-ray diffraction curve corresponding to the two-dimensional diffraction pattern was shown in Fig. 13. For isotropic PA6, the diffraction peak at

$2\theta=21.5^\circ$ was observed corresponding to the reflection of (200)/(001) of the γ crystal form. There were two new diffraction peaks for the oriented samples at $2\theta=20^\circ$ and 23° , which could be assigned to the reflection of (200) and (002)/(202) of the α crystal form of PA6, respectively. In addition, the intensity of the diffraction peaks at $2\theta=23^\circ$ increased with the draw ratio. The results indicated the transformation of γ crystalline form to α -form after drawn.

Fig. 13

The crystallinity of PA6 can be calculated by the peak area of crystal and amorphous region from the corresponding decomposed curves obtained by PeakFit software. Azimuthal scans ($0-360^\circ$) were performed for the characteristic reflections of PA6, and the Fit-2d package was employed to analyze the resultant 2D-WAXD patterns. The orientation factor (f) was calculated using Herman's orientation function [28-30]:

$$f = \frac{3 \langle \cos^2 f \rangle - 1}{2} \quad (11)$$

$$\langle \cos^2 \phi \rangle = \frac{\int_0^{\pi/2} I(\phi) \sin \phi \cos^2 \phi d\phi}{\int_0^{\pi/2} I(\phi) \sin \phi d\phi} \quad (12)$$

where $I(\phi)$ is the scattering intensity along the angle ϕ . The calculated data were summarized in Tab. 4.

When the grain size is below $10\mu\text{m}$, the polycrystal X-ray diffraction peak broadens remarkably. Based on the widen amount of diffraction peak, the grain size can be calculated with the following equation [31]:

$$L_{hkl} = \frac{k\lambda}{\beta \cos \theta} \quad (13)$$

where L_{hkl} is the grain size of normal direction of (hkl) crystal plane; θ is the Bragg

angle; β is the widening amount of diffraction peak attributed to the decrease of the grain size; λ is the wave length of entrance X-ray; k is a constant.

Tab. 4

As shown in Table 4, with the increase of the draw ratio, the crystallinity and oriented factor of PA6 increased, while the grain size of PA6 decreased, indicating that slipping and rupture of the lamellar in the spherulite occurred during the drawing of PA6 and a clear orientation of PA6 molecules formed.

Figure 14 shows the corresponding one-dimensional X-ray diffraction curves of PA6 as a function of aging time. It can be seen that phase transition from γ -to α -crystals occurred during hydrothermal aging. In the presence of moisture, the chains in the meta-stable γ -phase are sufficiently mobile to assume the more stable, lower energy conformation, hence partially converting them to the α -form. Compared with the isotropic sample, the oriented samples could keep relatively stable dense crystalline structure due to its formed α -form by drawn.

Fig. 14

The crystallinity, grain size and orientation factor calculated from the XRD scans as a function of aging time is shown in Fig. 15. The crystallinity and grain size of isotropic PA6 increased at the initial stage of aging, indicating the fact that post crystallization occurred as a result of the aging process. In addition, the hydrothermal degradation would primarily occur in the amorphous region of PA6, resulting in the increase of the crystalline region [32-33]. After 30 days of aging, the crystallinity and grain size decreased, ascribing to the degradation of crystallization regions after the complete degradation of the amorphous regions. In comparison, for the oriented sample, the crystallinity, grain size and orientation factor changed slightly with time, indicating that the oriented sample could keep relatively stable crystal orientation

structure. In this case, the orientation and crystalline domains played an important role in slowing down the hydrolysis.

Fig. 15

The glass transition temperature (T_g) of PA6 samples was measured by DMA analysis, and the results was shown in Fig. 16. For the isotropic sample of PA6, in the initial stage of aging, lots of water diffused into the PA6 matrix, functioning as plasticizer and resulting in a decrease of T_g , and after 20 days, a slight increase of T_g can be observed due to the increase of crystallinity and degradation of the amorphous region. The T_g of PA6 moved to higher temperatures with increasing of draw ratio, which indicated that the local motions of molecular chains in the amorphous region and defect region within the crystal were suppressed, and moreover the T_g for the oriented samples kept relatively stable during hydrothermal aging.

Fig. 16

3.2.3 The fractional free volume

Positron lifetime spectroscopy has been applied to investigate the structural changes of PA6 induced by tensile orientation and hydrothermal aging. To obtain the fractional free volume (f_v) and the hole radius (R), a semiempirical relationship between the ortho positronium atom (o-Ps) lifetime and the average radius of the free volume holes was used [34]:

$$\tau_3 = \frac{1}{2} \left[1 - \frac{R}{R_0} + \frac{1}{2\pi} \sin\left(\frac{2\pi R}{R_0}\right) \right]^{-1} \quad (14)$$

where R denotes the average radius of the free volume holes expressed in angstroms. R_0 is equal to $R + \Delta R$, and $\Delta R = 1.656 \text{ \AA}$ is the estimated empirical electron layer thickness. According to the calculated R from eq. (14), the average volume of the free volume holes can be obtained by using the spherical hole model, i.e., $V_h = 4\pi R^3/3$.

The free volume fraction can be estimated according to the following empirical formula:

$$f_v = AV_h I_3 \quad (15)$$

where A is an empirical parameter determined to be 0.0018 from specific volume data by Wang et al. [35] I_3 is the o-Ps intensity.

As shown in Tab. 5, compared with the isotropic PA6, the hole radius (R) changed slightly, and the fractional free volume (f_v) decreased for the oriented sample, resulting from the orientation of the amorphous region and the merger of the free volume hole. It can be seen that for the isotropic PA6, both f_v and R showed a decrease for the aged sample, indicating that the small molecules and low molecular weight PA6 produced by degradation in the amorphous region were suitable to join the polymeric crystallites, while a slight change occurred for oriented PA6. The second lifetime peak (I_2) of positrons was related with the crystalline/amorphous interfacial defects of the crystalline lamellae [36]. After aging, the intensity of I_2 for the isotropic PA6 increased, indicating the increase of the defects in crystalline region, while a slight change of I_2 and a more stable structure were observed for the oriented sample of PA6.

Tab. 5

4. Conclusion

Highly oriented PA6 was successfully fabricated through solid hot stretching technology. The effect of orientation on the structure and hydrothermal stability of PA6 was investigated. It was found that with the increase of draw ratio, the crystallinity and orientation factor of PA6 increased, and micro-fibre structure was formed, while the hydrophilic property was weakened. During hydrothermal aging,

the equilibrium water absorption ratio and diffusion coefficient (D) of water decreased with the increase of draw ratio, and the oriented samples kept relatively higher reduced viscosity and mechanical property. The sample became yellowing and surface cracked during aging, which were remarkably reduced by orientation. The enhancing mechanism of hydrothermal stability of PA6 was explored, and the stable dense crystalline structure with α crystal form formed by orientation contributed to slowing down the hydrolytic degradation.

Acknowledgements

This study was financially supported by the Key Natural Science Foundation of China (Grant No. 51133005).

Reference

- [1] Li L, Yang G. Variable-temperature FTIR studies on thermal stability of hydrogen bonding in nylon 6/mesoporous silica nanocomposite. *Polymer International* **2009**, 58, 503-10.
- [2] Hu Z, Chen L, Lin G-P, Luo Y, Wang Y-Z. Flame retardation of glass-fibre-reinforced polyamide 6 by a novel metal salt of alkylphosphinic acid. *Polymer Degradation and Stability* **2011**, 96, 1538-45.
- [3] Gonçalves ES, Poulsen L, Ogilby PR. Mechanism of the temperature-dependent degradation of polyamide 66 films exposed to water. *Polymer Degradation and Stability* **2007**, 92, 1977-85.

- [4] El-Mazry C, Correc O, Colin X. A new kinetic model for predicting polyamide 6-6 hydrolysis and its mechanical embrittlement. *Polymer Degradation and Stability* **2012**, 97, 1049-59.
- [5] Shu Y, Li X, Ye L. Study on the Long-Term Acid Rain Aging Behaviour of Polyamide 6. *Journal of Macromolecular Science, Part B* **2009**, 48, 526-36.
- [6] Murthy N S, Stamm M, Sibilica J P, et al. Structural changes accompanying hydration in nylon 6. *Macromolecules* **1989**, 22(3), 1261-1267.
- [7] Vlasveld D P N, Groenewold J, Bersee H E N, et al. Moisture absorption in polyamide-6 silicate nanocomposites and its influence on the mechanical properties. *Polymer* **2005**, 46(26), 12567-12576.
- [8] Yang T, Ye L, Shu Y. Thermal stabilization effect of biphenol monoacrylate on polyamide 6. *Journal of applied polymer science* **2008**, 110(2), 856-863.
- [9] Shi K, Ye L. In situ stabilization of polyamide 6 with reactive antioxidant. *Journal of Thermal Analysis and Calorimetry* **2015**, 119, 1747-57.
- [10] Forsström D, Terselius B. Thermo oxidative stability of polyamide 6 films I. Mechanical and chemical characterisation. *Polymer degradation and stability* **2000**, 67(1), 69-78.
- [11] Shi K, Ye L. Photo-Oxidative Stabilization Effect of a Reactive Hindered Amine on Monomer Casting Nylon-6. *Journal of Macromolecular Science, Part B* **2014**, 53(8), 1453-1464.

- [12] Eldsäter C, Erlandsson B, Renstad R, Albertsson AC, Karlsson S. The biodegradation of amorphous and crystalline regions in film-blown poly(ϵ -caprolactone). *Polymer* **2000**, 41, 1297-304.
- [13] Cho DK, Park JW, Kim SH, Kim YH, Im SS. Effect of molecular orientation on biodegradability of poly(glycolide-co- ϵ -caprolactone). *Polymer Degradation and Stability* **2003**, 80, 223-32.
- [14] Zhou Y, Dan Y, Jiang L, Li G. The effect of crystallization on hydrolytic stability of polycarbonate. *Polymer Degradation and Stability* **2013**, 98, 1465-72.
- [15] Solomon OF, Ciută IZ. Détermination de la viscosité intrinsèque de solutions de polymères par une simple détermination de la viscosité. *Journal of Applied Polymer Science* **1962**, 6, 683-6.
- [16] Campoy I, Gomez M A, Marco C. Structure and thermal properties of blends of nylon 6 and a liquid crystal copolyester. *Polymer* **1998**, 39(25), 6279-6288.
- [17] Wiggins J S, Hassan M K, Mauritz K A, et al. Hydrolytic degradation of poly (d, l-lactide) as a function of end group: carboxylic acid vs. hydroxyl. *Polymer* **2006**, 47(6), 1960-1969.
- [18] Tham W, Ishak ZM, Chow W. Water Absorption and Hygrothermal Aging Behaviors of SEBS-g-MAH Toughened Poly (lactic acid)/Halloysite Nanocomposites. *Polymer-Plastics Technology and Engineering* **2014**, 53, 472-80.
- [19] Gonçalves ES, Poulsen L, Ogilby PR. Mechanism of the temperature-dependent degradation of polyamide 66 films exposed to water. *Polymer Degradation and Stability* **2007**, 92, 1977-85.

- [20] Pitt CG, Zhong-wei G. Modification of the rates of chain cleavage of poly(ϵ -caprolactone) and related polyesters in the solid state. *Journal of Controlled Release* **1987**, 4, 283-92.
- [21] Zhou Q, Xanthos M. Nanoclay and crystallinity effects on the hydrolytic degradation of polylactides. *Polymer Degradation and Stability* **2008**, 93, 1450-9.
- [22] Li R, Hu X. Study on discoloration mechanism of polyamide 6 during thermo-oxidative degradation. *Polymer Degradation and Stability* **1998**, 62, 523-8.
- [23] Zhao N, Weng L, Zhang X, Xie Q, Zhang X, Xu J. A Lotus-Leaf-Like Superhydrophobic Surface Prepared by Solvent-Induced Crystallization. *Chemphyschem : a European journal of chemical physics and physical chemistry* **2006**, 7, 824-7.
- [24] Wenzel RN. Resistance of solid surfaces to wetting by water. *Industrial & Engineering Chemistry* **1936**, 28, 988-94.
- [25] Herminghaus S. Roughness-induced non-wetting. *EPL (Europhysics Letters)* **2000**, 52, 165.
- [26] Zhao X, Ye L. Structure and properties of highly oriented polyoxymethylene produced by hot stretching. *Materials Science and Engineering: A* **2011**, 528(13), 4585-4591.
- [27] Holmes D, Bunn C, Smith D. The crystal structure of polycaproamide: Nylon 6. *Journal of polymer Science* **1955**, 17, 159-77.
- [28] Zhang X, Shi F, Niu J, et al. Superhydrophobic surfaces: from structural control to functional application. *Journal of Materials Chemistry* **2008**, 18(6), 621-633.

- [29] Rungswang W, Plailahan K, Saendee P, et al. Tensile deformation of in-reactor polymer alloy with preferentially oriented crystallite in parallel and perpendicular to uniaxial stretching direction: A model case from impact-resistance polypropylene copolymer. *Polymer* **2013**, 54(14), 3699-3708.
- [30] Liu Q, Sun X, Li H, et al. Orientation-induced crystallization of isotactic polypropylene. *Polymer* **2013**, 54(17), 4404-4421.
- [31] Fourati M, Pellerin C, Bazuin C G, et al. Infrared and fluorescence spectroscopy investigation of the orientation of two fluorophores in stretched polymer films. *Polymer* **2013**, 54(2), 730-736.
- [32] Luo Y-B, Wang X-L, Wang Y-Z. Effect of TiO₂ nanoparticles on the long-term hydrolytic degradation behavior of PLA. *Polymer Degradation and Stability* **2012**, 97, 721-8.
- [33] Rangari D, Vasanthan N. Study of Strain-Induced Crystallization and Enzymatic Degradation of Drawn Poly(l-lactic acid) (PLLA) Films. *Macromolecules* **2012**, 45, 7397-403
- [34] Eldrup M, Lightbody D, Sherwood JN. The temperature dependence of positron lifetimes in solid pivalic acid. *Chemical Physics* **1981**, 63, 51-8.
- [35] Wang YY, Nakanishi H, Jean YC, Sandreczki TC. Positron annihilation in amine-cured epoxy polymers—pressure dependence. *Journal of Polymer Science Part B: Polymer Physics* **1990**, 28, 1431-41.

[36] Monge MA, Díaz JA, Pareja R. Strain-Induced Changes of Free Volume Measured by Positron Lifetime Spectroscopy in Ultrahigh Molecular Weight Polyethylene. *Macromolecules* **2004**, 37, 7223-30.

Table captions

Tab. 1 The diffusion rate of water in PA6 matrix with different draw ratio

Tab. 2 Auto-catalyzed hydrolytic degradation rate constants and the corresponding R correlation coefficients of PA6 with different draw ratio

Tab. 3 DSC parameters of PA6 with different draw ratio

Tab. 4 Crystallinity, orientation factor and grain size of PA6 with different draw ratio

Tab. 5 Intensity of I_2 and I_3 , f_v and R for PA6 with different draw ratio

Figure captions

Fig. 1 Water absorption of PA6 with different draw ratio as a function of hydrothermal aging time

Fig. 2 The plot of water absorption versus $t^{1/2}/L$ for PA6 during hydrothermal aging

Fig. 3 Weight gain of PA6 with different draw ratio as a function of hydrothermal aging time

Fig. 4 Intrinsic viscosity of PA6 as a function of hydrothermal aging time

Fig. 5 $\ln([\eta]/[\eta]_0)$ of PA6 as a function of hydrothermal aging time

Fig. 6 Retention of the mechanical properties of PA6 with different draw ratio as a function of hydrothermal aging time

Fig. 7 The surface appearance of PA6 with different draw ratio during the hydrothermal aging

Fig. 8 SEM images of PA6 with different draw ratio during the hydrothermal aging (Magnification: 1000 \times)

Fig. 9 Water contact angles of PA6 as a function of draw ratio

Fig. 10 Crystalline morphology of etched surface of PA6 with different draw ratio

(Magnification: 200×)

Fig. 11 DSC curves of PA6 with different draw ratio

Fig. 12 2D-XRD patterns of PA6 with different draw ratio at different hydrothermal aging time

Fig. 13 WAXD curves of PA6 with different draw ratio

Fig. 14 WAXD curves of PA6 with different draw ratio at different hydrothermal aging time

Fig. 15 Grain size, crystallinity and orientation factor of PA6 as a function of hydrothermal aging time

Fig. 16 Glass transition temperature (T_g) of PA6 as a function of hydrothermal aging time

Tab. 1 The diffusion rate of water in PA6 matrix with different draw ratio

Draw ratio (%)	0	200	400	600
M_{∞} (%)	8.75	7.84	6.72	6.12
D (mm ² /s)	9.89×10^{-5}	2.40×10^{-5}	1.02×10^{-5}	7.12×10^{-6}

Tab. 2 Auto-catalyzed hydrolytic degradation rate constants and the corresponding R correlation coefficients of PA6 with different draw ratio

Draw ratio (%)	0	200	400	600
$K_1 \times 10^3/\text{day}^{-1}$	10.04	8.94	6.36	3.98
R^2	0.97	0.97	0.97	0.96

Tab. 3 DSC parameters of PA6 with different draw ratio

Draw ratio (%)	T_m (°C)	ΔH (J/g)	Crystallinity (%)	Left Area (%)	Right Area (%)
0	223.3	74.56	39.24	23.31	76.69
200	221.9	85.44	44.97	—	—
400	221.1	86.31	45.42	—	—
600	221.1	101.9	53.63	—	—

Tab. 4 Crystallinity, orientation factor and grain size of PA6 with different draw ratio

Draw ratio (%)	Crystallinity (%)	Orientation factor	Grain size (Å)
0	42.35	—	38
200	58.52	0.17	24
400	59.07	0.18	22
600	62.11	0.21	27

Tab. 5 Intensity of I_2 and I_3 , f_v and R for PA6 with different draw ratio

Time/d	Draw ratio (%)	I_2 (%)	I_3 (%)	τ_3 (ps)	R (nm)	f_v
0	0	58.45	20.92	1.64	0.2500	2.463×10^{-3}
	400	61.13	19.17	1.65	0.2507	2.277×10^{-3}
42	0	60.40	19.61	1.61	0.2461	2.203×10^{-3}
	400	61.12	18.99	1.63	0.2481	2.185×10^{-3}

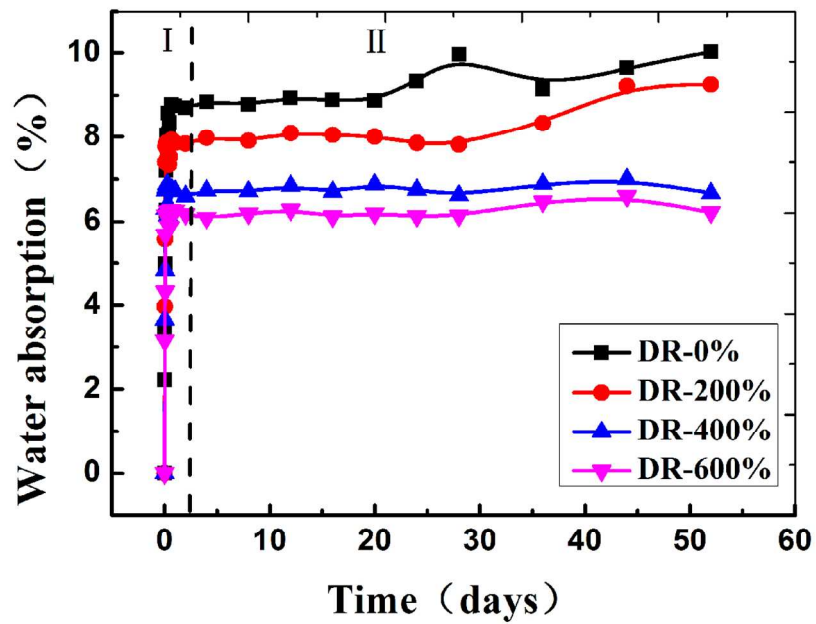


Fig. 1 Water absorption of PA6 with different draw ratio as a function of hydrothermal aging time
127x89mm (300 x 300 DPI)

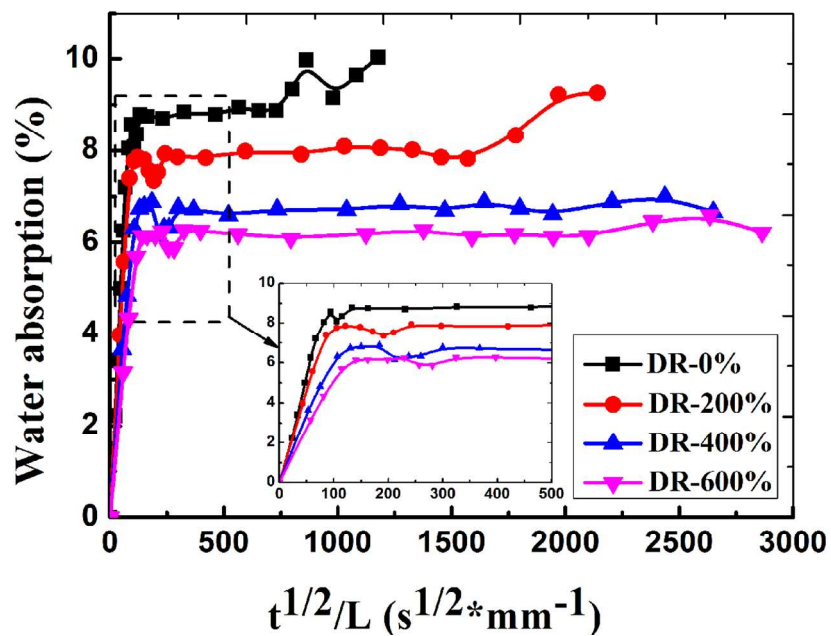


Fig. 2 The plot of water absorption versus $t^{1/2}/L$ for PA6 during hydrothermal aging
127x89mm (300 x 300 DPI)

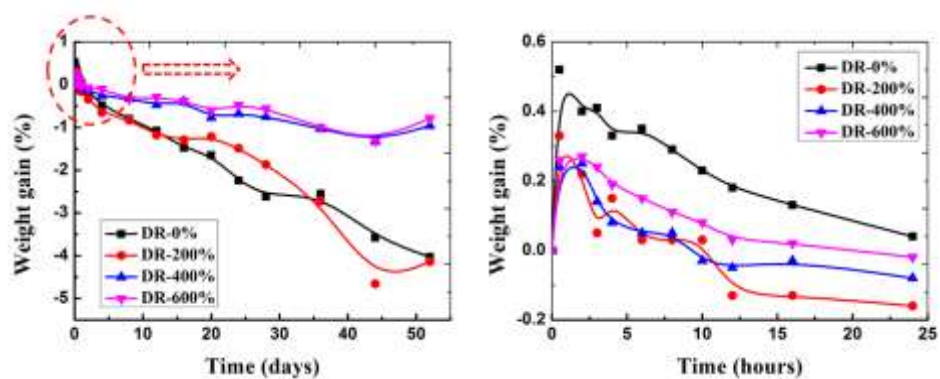


Fig. 3 Weight gain of PA6 with different draw ratio as a function of hydrothermal aging time
254x98mm (150 x 150 DPI)

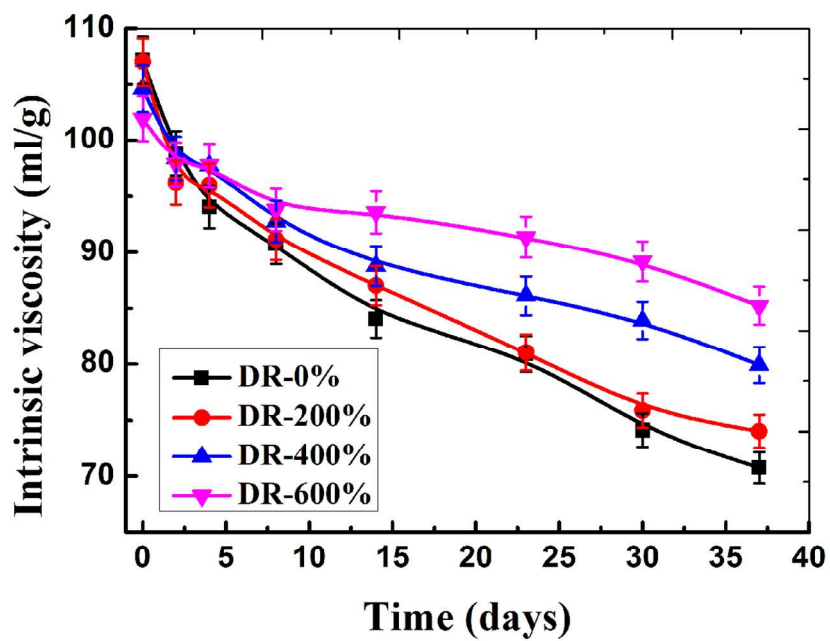


Fig. 4 Intrinsic viscosity of PA6 as a function of hydrothermal aging time
127x89mm (300 x 300 DPI)

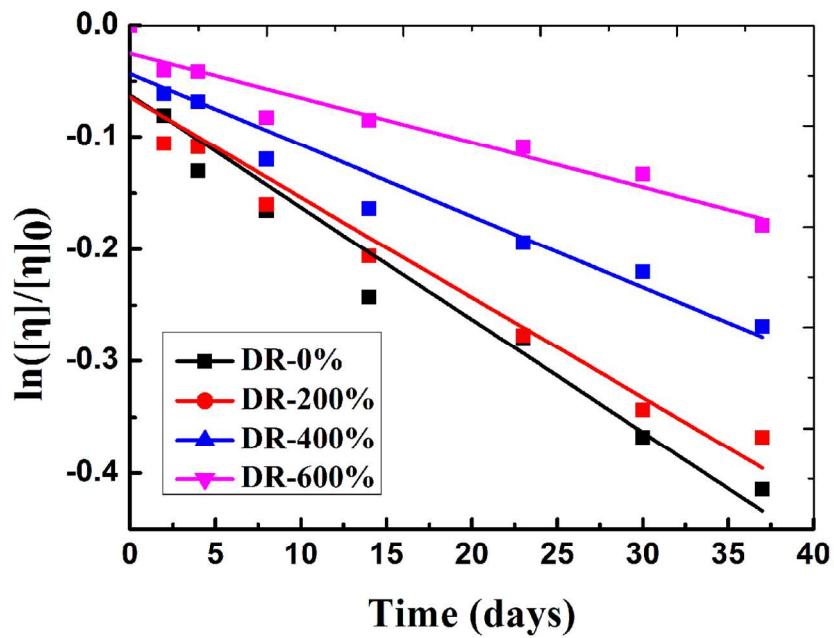


Fig. 5 $\ln([\eta]/[\eta]_0)$ of PA6 as a function of hydrothermal aging time
127x89mm (300 x 300 DPI)

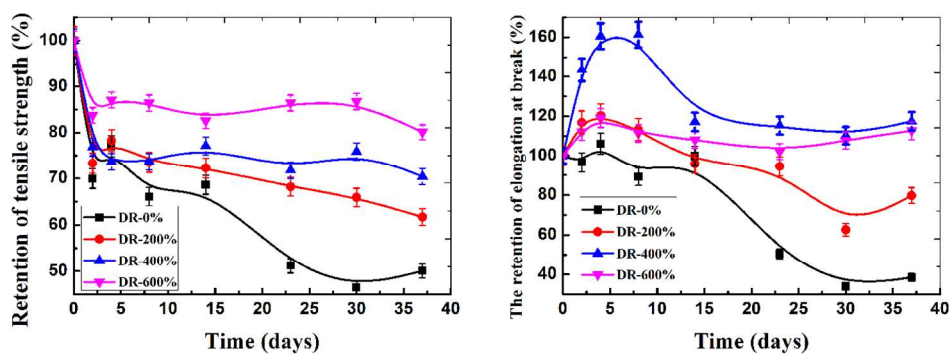


Fig. 6 Retention of the mechanical properties of PA6 with different draw ratio as a function of hydrothermal aging time
127x49mm (300 x 300 DPI)

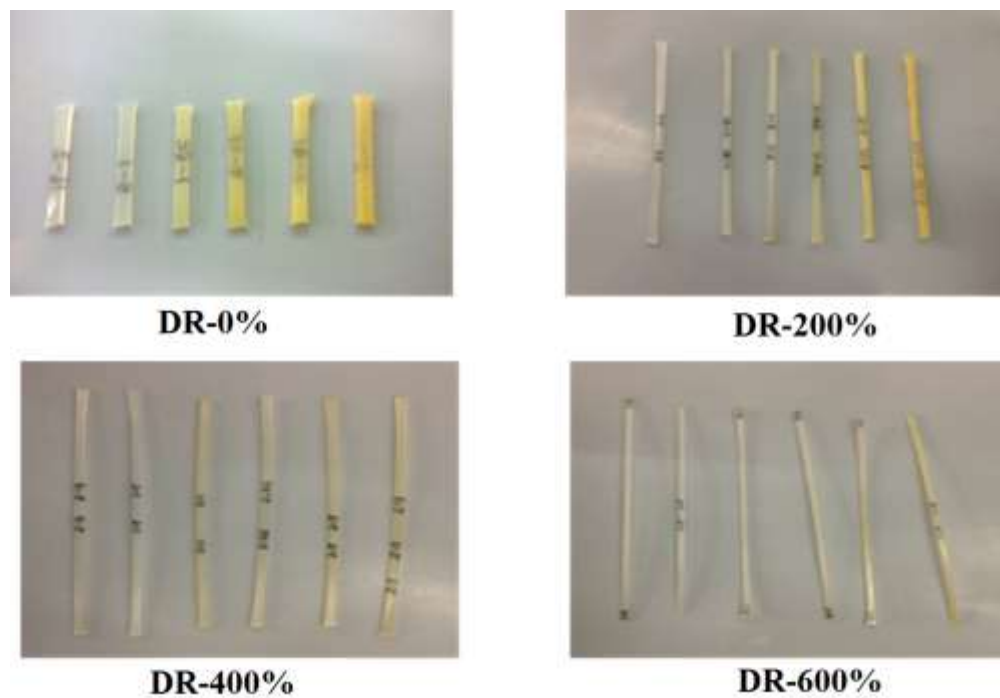


Fig. 7 The surface appearance of PA6 with different draw ratio during the hydrothermal aging 396x280mm (96 x 96 DPI)

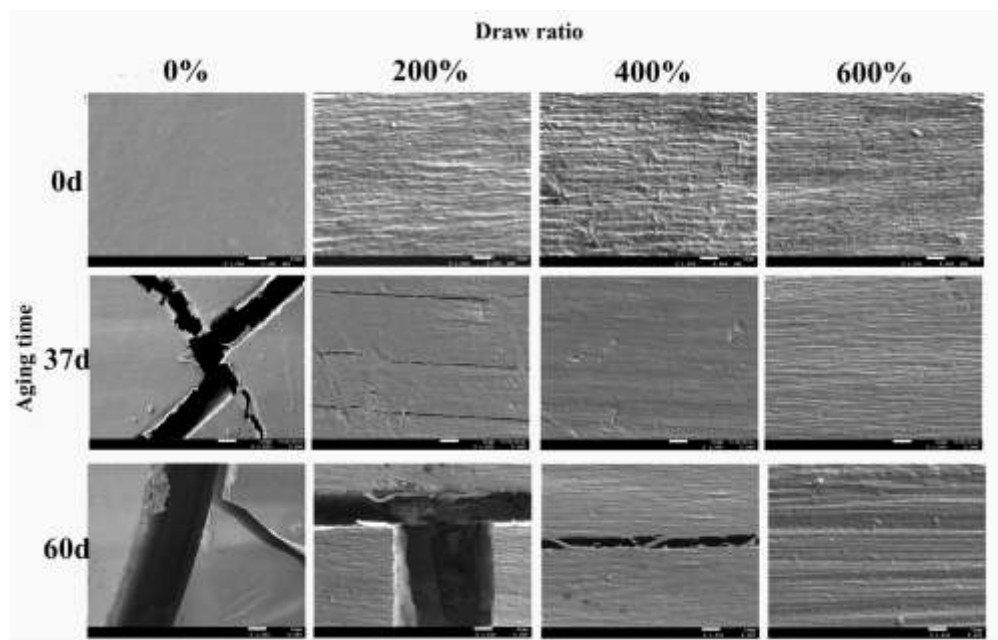


Fig. 8 SEM images of PA6 with different draw ratio during the hydrothermal aging (Magnification: 1000×)
141x89mm (270 x 270 DPI)

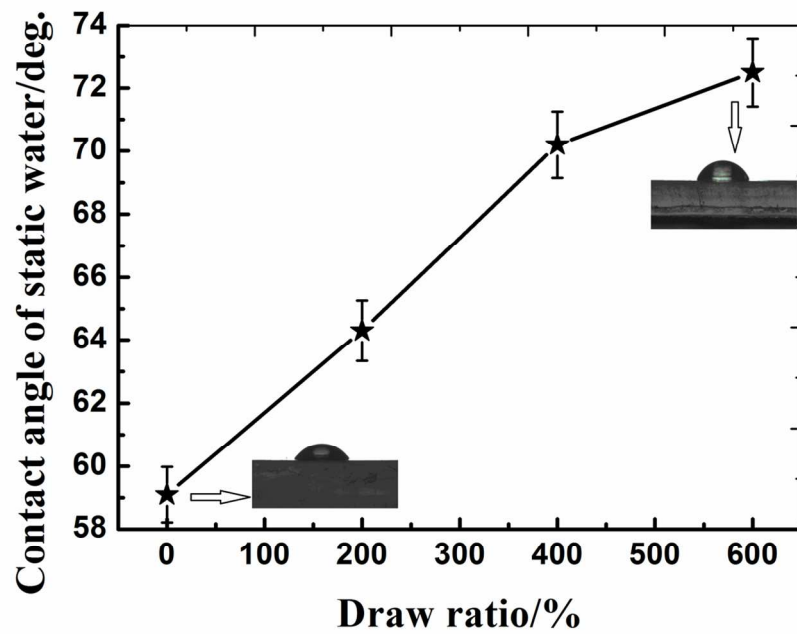


Fig. 9 Water contact angles of PA6 as a function of draw ratio
127x89mm (299 x 299 DPI)

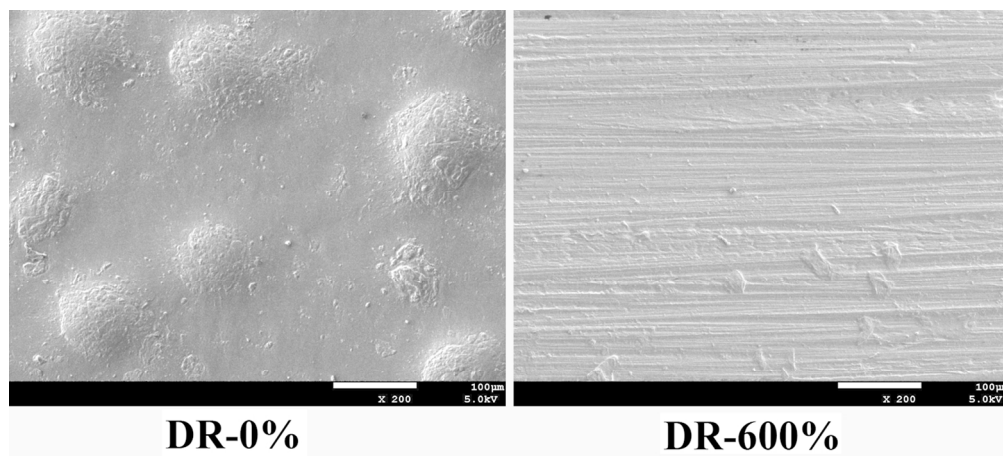


Fig. 10 Crystalline morphology of etched surface of PA6 with different draw ratio (Magnification: 200×)
140x63mm (271 x 271 DPI)

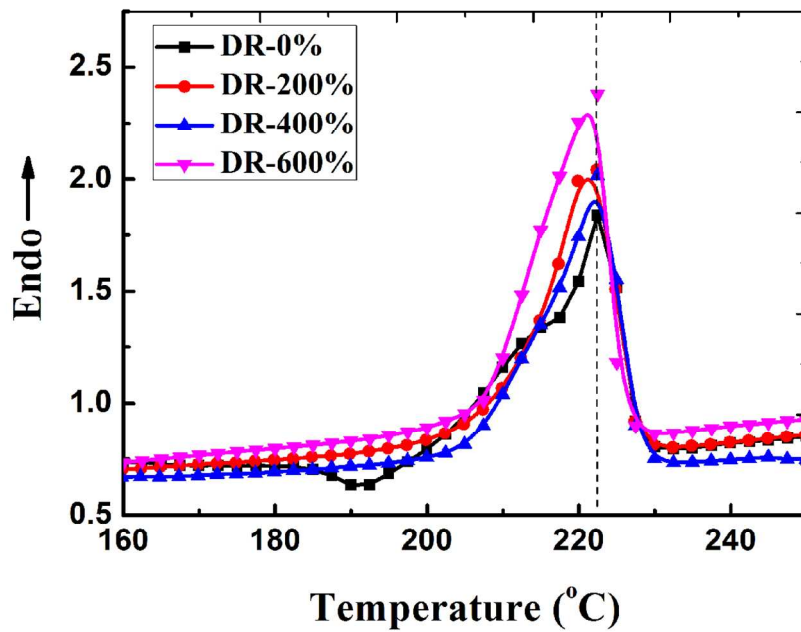


Fig. 11 DSC curves of PA6 with different draw ratio
127x89mm (300 x 300 DPI)

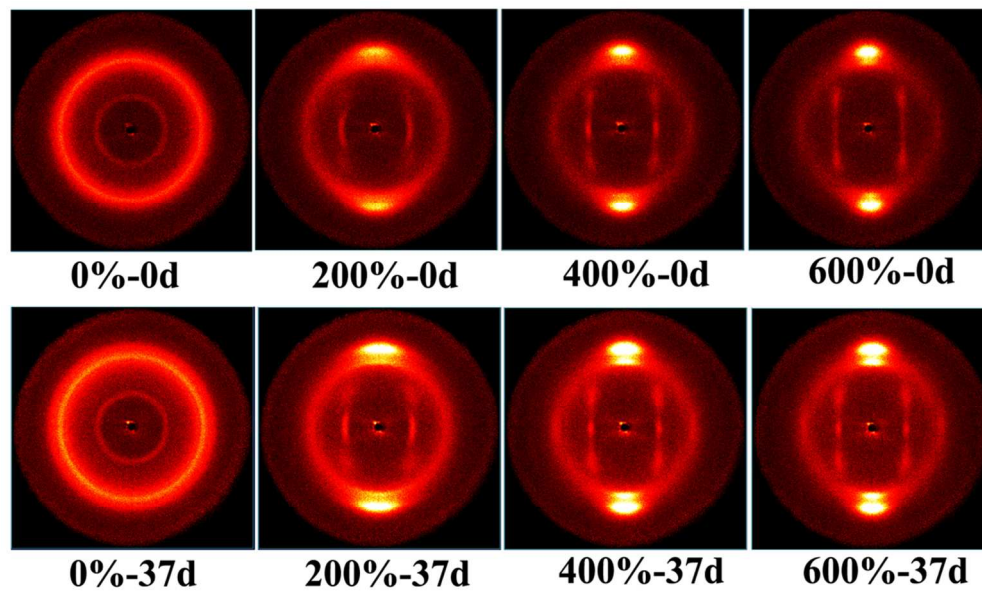


Fig. 12 2D-XRD patterns of PA6 with different draw ratio at different hydrothermal ageing time
173x105mm (219 x 219 DPI)

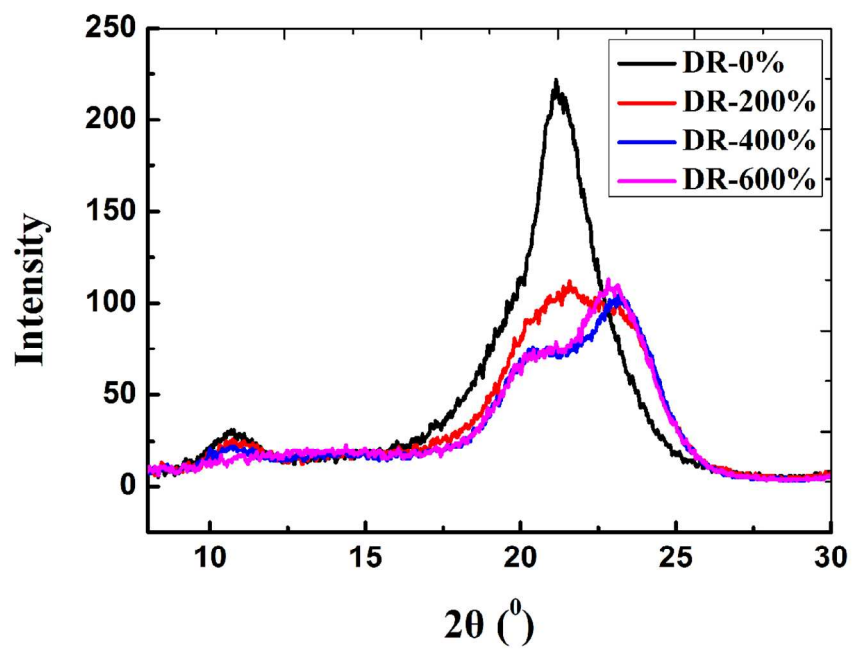


Fig. 13 WAXD curves of PA6 with different draw ratio
127x89mm (300 x 300 DPI)

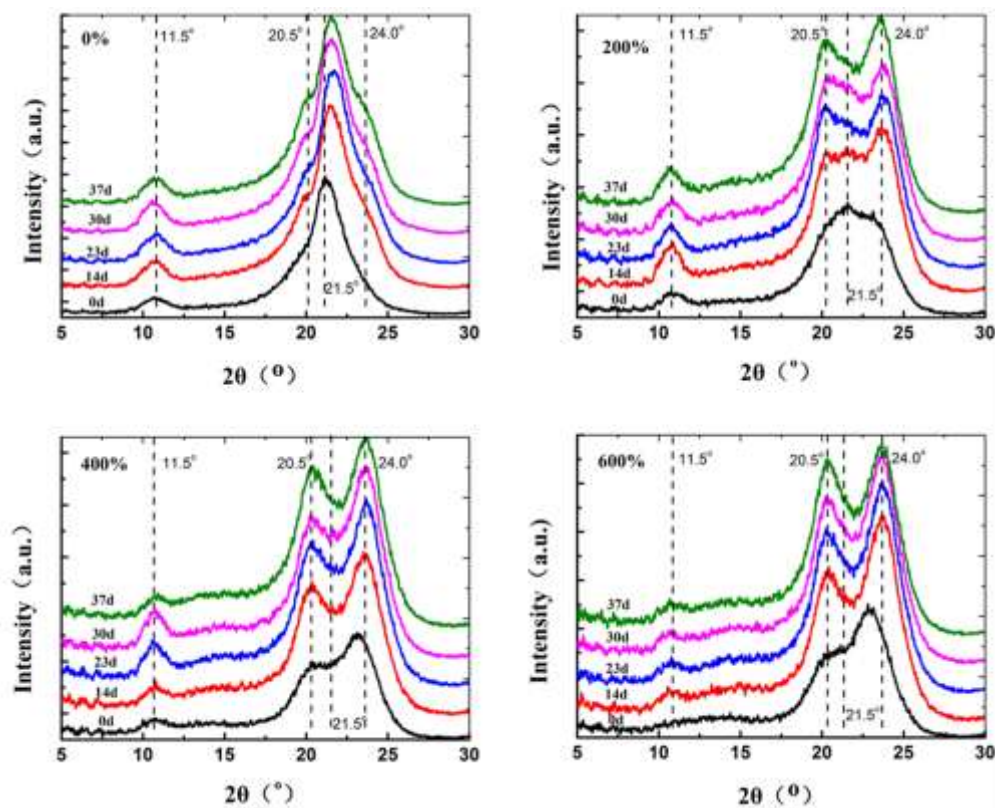


Fig. 14 WAXD curves of PA6 with different draw ratio at different hydrothermal ageing time
255x204mm (149 x 149 DPI)

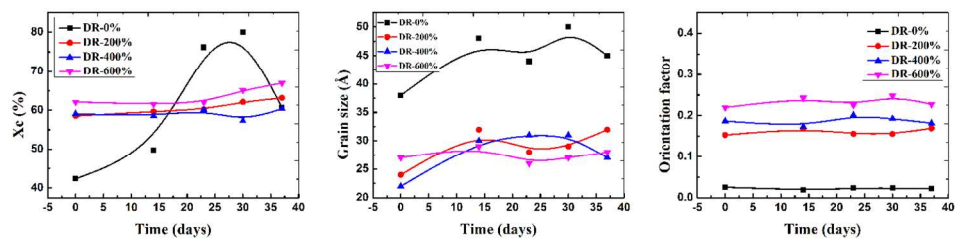


Fig. 15 Grain size, crystallinity and orientation factor of PA6 as a function of hydrothermal aging time 127x32mm (300 x 300 DPI)

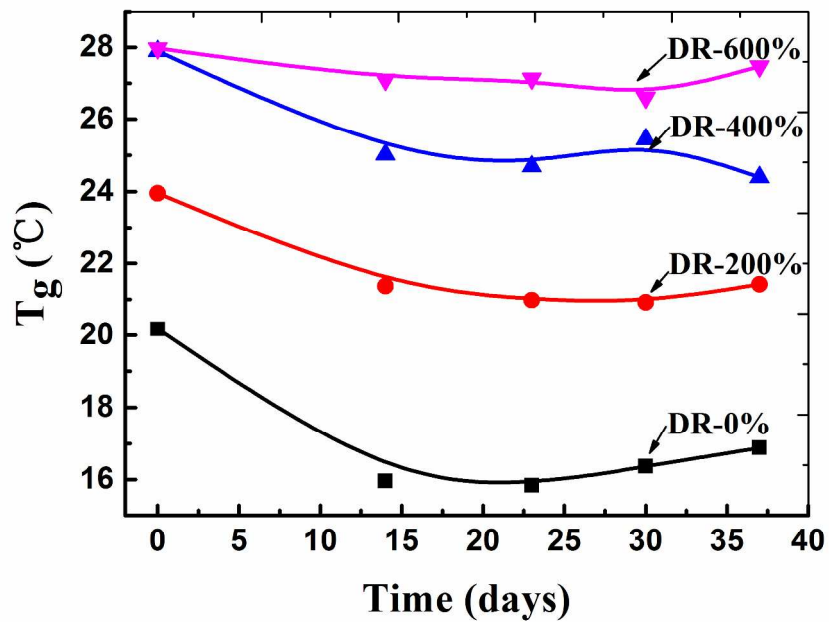


Fig. 16 Glass transition temperature (T_g) of PA6 as a function of hydrothermal aging time
287x201mm (300 x 300 DPI)